Supplement of Atmos. Chem. Phys., 26, 247–268, 2026
https://doi.org/10.5194/acp-26-247-2026-supplement

Atmospheric Chemistry and Physics
Open Access
EGU

Supplement of

Decadal trends (2013–2023) in PM_{10} sources and oxidative potential at a European urban supersite (Grenoble, France)

Vy Ngoc Thuy Dinh et al.

Correspondence to: Gaëlle Uzu (gaelle.uzu@ird.fr)

Supplement information

S1. Multivariate imputation by chained equations (MICE)

Multivariate imputation by chained equations (MICE) is a flexible algorithm that could be combined with other statistical techniques for estimating missing values by using observed data (by performing the linear, multilinear regression or calculation of the mean/median to fill the missing) (Azur et al., 2011). The MICE algorithm employs multiple regression models, where each missing value is conditionally modeled based on the observed (non-missing) values. This imputation process provides a more complete database for PMF analysis, contributing to a reduction in recommendation errors in the results (Ocepek et al., 2015).

Here, the data preparation and imputation processes were implemented through 4 main steps. First, all missing values of each metal are replaced by the mean of its concentration, these replaced values are marked as "place-holders". Second step, the metal that has the fewest missing values was chosen, and the "place-holder" is put back to missing (called Px). In the third step, a multiple linear regression is applied, with the chosen metal set as a criterion and the other variables are predictors. Fourth step, the missing value Px is calculated by using the slope and intercepts of multiple linear regression in the third step. The processes between the second and the fourth steps are repeated until all "place-holders" are replaced by the regression prediction value; this repeated run is called the "cycle" of imputation. The imputation cycle is iterative implemented until the difference between the 2 last cycles is minimized. MICE was implemented in Python 3.9 using the package "*scikit-learn 1.2.0*" (Pedregosa et al., 2011).

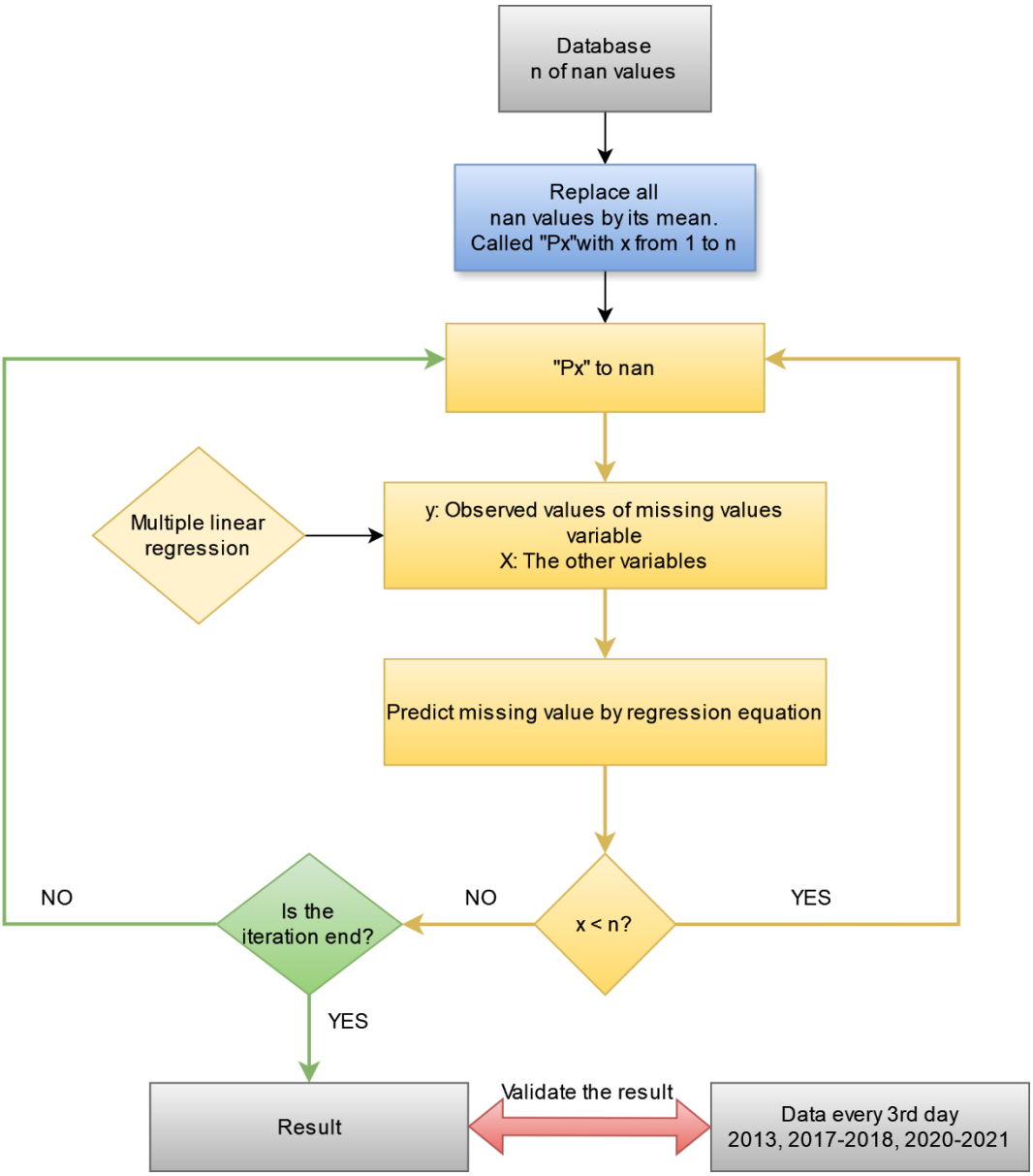

Figure S1. Workflow of the MICE algorithm

Table S 1. R^2 between imputed and measured metals

	2013	2017-2018	2020-2021
As	0.43	0.6	0.2
Cd	0.41	0.55	0.1
Cr	0.32	0.34	0.38
Cu	0.63	0.4	0.42
Mn	0.33	0.35	0.5
Ni	0.14	0.33	0.14
Pb	0.33	0.31	0.15
Sb	0.37	0.50	0.2
V	0.41	0.27	0.52
Zn	0.26	0.35	0.20

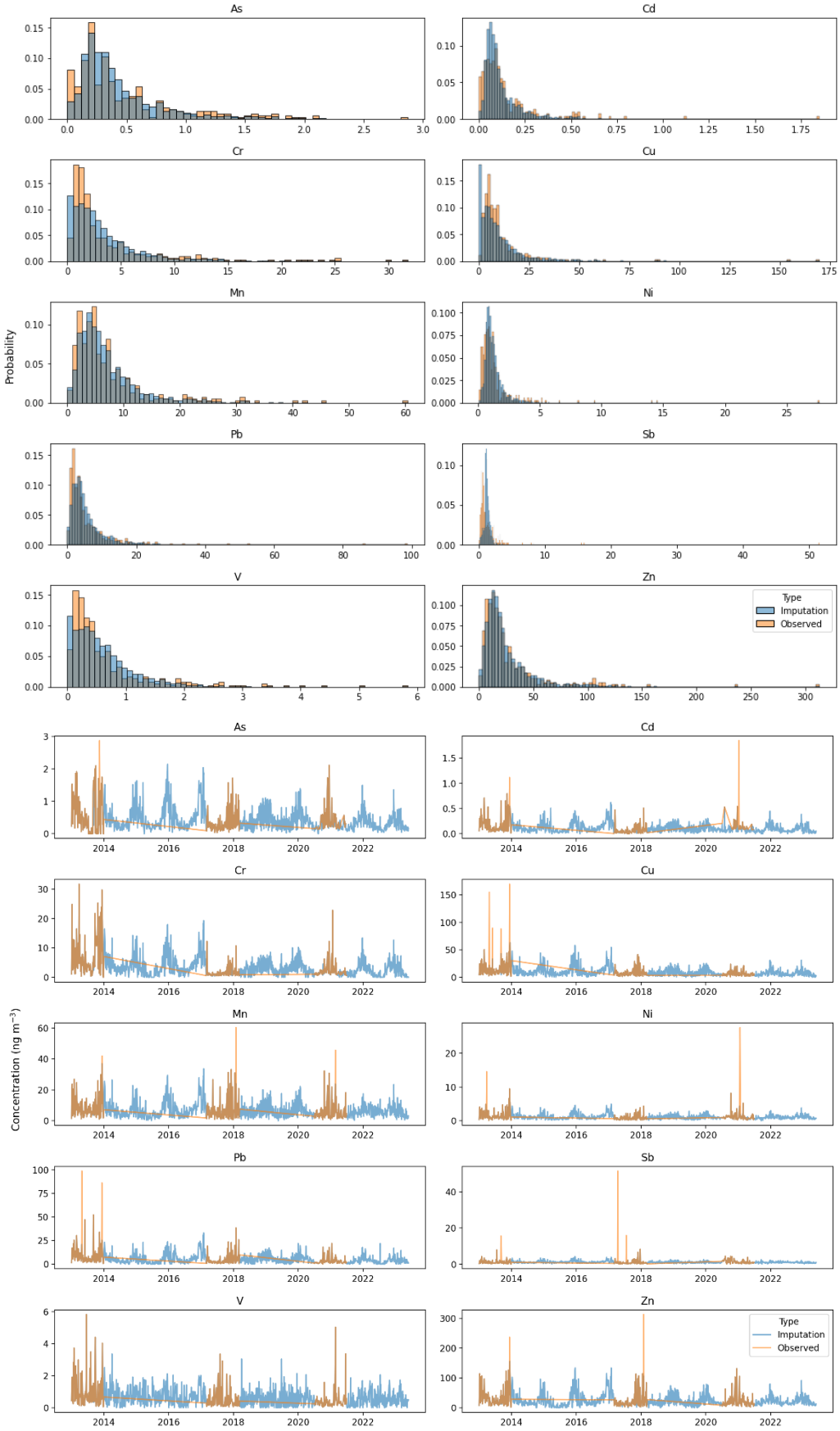

Figure S2. Distribution (upper) and temporal evolution (lower) of measured and imputed metals

S2. Some equations

PMF equation:

$$X_{ij} = \sum_{k=1}^{p} G_{ik} * F_{kj} + E_{ij} \quad (Eq.(S1))$$

$$G_{ik} \geq 0,\ F_{ik} \geq 0 \ (Eq.(S2))$$

Where X is a (i × j) matrix of j chemical species in measured period i (daily) into p factors with a matrix (i x k) representing the source contribution (G) and a matrix (k x j) representing the factor composition (F). E is the residuals for each species. All the factor matrices G and F elements are constrained to be non-negative.

Variance Inflation Factor (VIF) represent the collinearity between the PM sources, which is calculated:

$$VIF_i = \frac{1}{1 - R_i^2}, i = 1, \ldots, p - 1 \ (Eq.(S3))$$

Chemical Mass Closure:

$$PM10 \approx EC + OM + [sea\ salt] + [nss\text{-}SO_4^{2-}] + [dust] + [non\ dust]$$

with:

[OM] = [OC]*1.8 (Favez et al., 2010)

[sea salt] = $[Na^+]$*1.47 + [Cl-] (Putaud et al., 2010)

[nss-SO42-] = $[SO_4^{2-}]$ – $[Na^+]$*0.252 (Alexander et al., 2005)

[dust] = 5.6 * ($[Ca^{2+}]$ – $[Na^+]$/26) (Putaud et al., 2004)

[non dust] = [Cu] + [Pb] + [V] + [Zn] (Salameh et al., 2015)

S3. PMF input matrices

The basic chemical species to be included in the input matrices are key components for the mass balance of the PM: organic carbon (OC), element carbon (EC), major ions (nitrate, sulfate, ammonium), sea salt species (Na, Cl, Mg), and mineral dust (Al, Fe, Ti). Then the input matrices should include a set of chemical tracers that allows the discrimination of their sources. This list is very variable according to the analytical capabilities used in the research program.

In other to avoid double counting of carbon mass in OC and in organic tracers added to the input data (ie levoglucosan, mannosan, MSA, polyols in the classic PMF at IGE), we calculate a variable OC* by:

[OC*] = [OC] – [total mass C of organic tracers in PMF]

Uncertainties of measured data

A table of the uncertainties of each daily data for each chemical species should be constructed. Several ways for their calculations exist. Here, we are using the formula described in the table below, resulting from all the work developed in the SOURCE program and the post-doc work of D Salameh (published in Weber et al., 2019).

Table S 2. Formula to calculate uncertainties

Specie	Calculation by	Formula
OC*, EC, PM10	Fixed percentage	10%

Specie which has concentration < QL	Ratio of QL Polissar et al. (1998)	$\frac{5 \times QL}{6}$
Imputed metals	Gianini et al., 2012	$\sigma_{ij} = 2 * \sqrt{QL_j^2 + (CV_j \times x_{ij})^2 + \left(a \times x_{ij}\right)^2}$
The others	Gianini et al., 2012	$\sigma_{ij} = \sqrt{QL_j^2 + (CV_j \times x_{ij})^2 + \left(a \times x_{ij}\right)^2}$

With:

- QL : Quantification limit.
- CV : Coefficient of variation.
- a: Additional coefficient of variation
- x: Species concentration.

S4. PMF criteria for validation and applied constraint

According to the European guide on air pollution source apportionment with receptor models (Belis et al., 2014), the validation criteria of a PMF solution include:

(1) Evolution of Q_{true}/Q_{robust} < 1.5: Indicate that the good result should not have more than 30% data outliers. Generally, the final solution presents a much lower ratio.

(2) The chemical profile is clear: the concentration and percentage of trace species in the profile and the temporal variability should be clear enough to identify a source.

(3) All factors should have a contribution > 1% to the total variable (PM10): to avoid a case where there is a source, but it has almost no impact on the study area.

(4) The distribution of residuals: the distribution of residuals (differences between input data and reconstructed data) is from -3 to 3, if there is any value is out of this range, that means that the reconstruction is not valid or that there are outliers.

(5) Evaluate the species reconstruction: The correlation coefficient between measured and predicted concentrations must be greater than 0.5.

(6) Bootstrap test: it indicates the stability of the solution: at least 70 runs per 100 runs for all factors where the correlation between the base run and boot runs is greater than 0.6.

Table S 3. The constraints applied for PMF

Factor	Element	Type	Value
Industrial	Levoglucosan	Set to Zero	0
Industrial	Mannosan	Set to Zero	0
Industrial	PM10	Define Limits	0.1/0.4
MSA rich	MSA	Pull Up Maximally	NA
MSA rich	Polyols	Set to Zero	0
Biomass burning	Levoglucosan	Pull Up Maximally	NA
Biomass burning	Mannosan	Pull Up Maximally	NA
Primary biogenic	Polyols	Pull Up Maximally	NA
Primary traffic	Ba	Pull Up Maximally	NA

Primary traffic	Cu	Pull Up Maximally	NA
Primary traffic	OC*/EC	Ratio	0.44
Primary traffic	Cu/Sb	Ratio	12.6
Primary traffic	Cu/Mn	Ratio	5.7

S5. PMF results

Table S 4. Q_{true}/Q_{robust} values

	10 yeas	2013-2016	2017-2020	2021-2023
Base run	1.07	1.05	1.05	1.1
Constraint run	1.07	1.06	1.05	1.1

Table S 5. Bootstrap value before and after constraint

	10 yeas		2013-2016		2017-2020		2021-2023	
	Base	Constraint	Base	Constraint	Base	Constraint	Base	Constraint
Aged sea salt	100	100	100	100	100	100	100	100
Biomass burning	100	100	100	100	100	100	100	100
Industrial	100	100	100	100	100	100	100	100
MSA rich	100	100	97	100	100	100	93	100
Mineral dust	100	100	93	100	98	100	85	100
Nitrate rich	100	100	100	100	100	100	100	100
Primary biogenic	100	100	100	100	100	100	100	100
Primary traffic	80	98	82	96	93	100	70	88
Chloride rich	98	100	99	100	92	100	99	100
Sulfate rich	100	100	87	99	98	100	96	95

Table S 6. R2 between observed and predicted by PMF of PM concentration

	10 yeas	**2013-2016**	**2017-2020**	**2021-2023**
Base run	0.97	0.98	0.97	0.98
Constraint run	0.97	0.98	0.97	0.98

Displacement run: No warning for unstable or un-useable solution for PMF performed on 10-years dataset and every 3 years datasets.

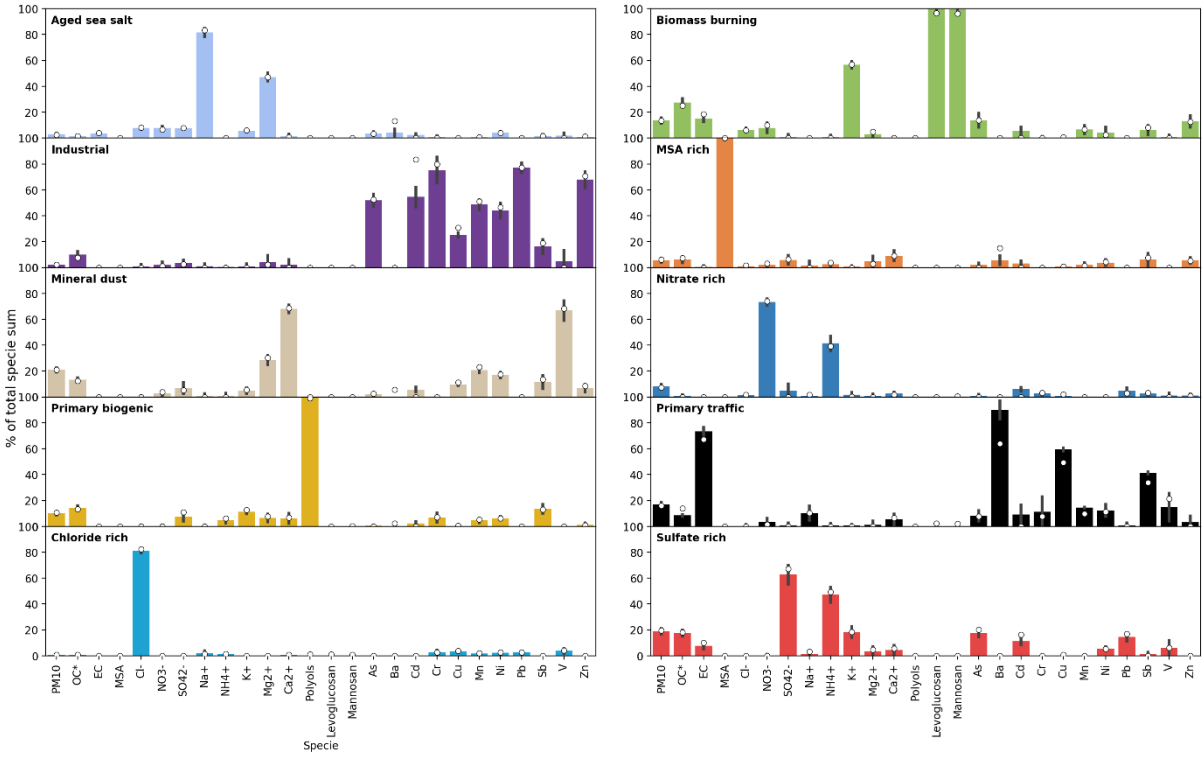

Figure S3. Chemical profiles of PM_{10} sources, solution 11 years

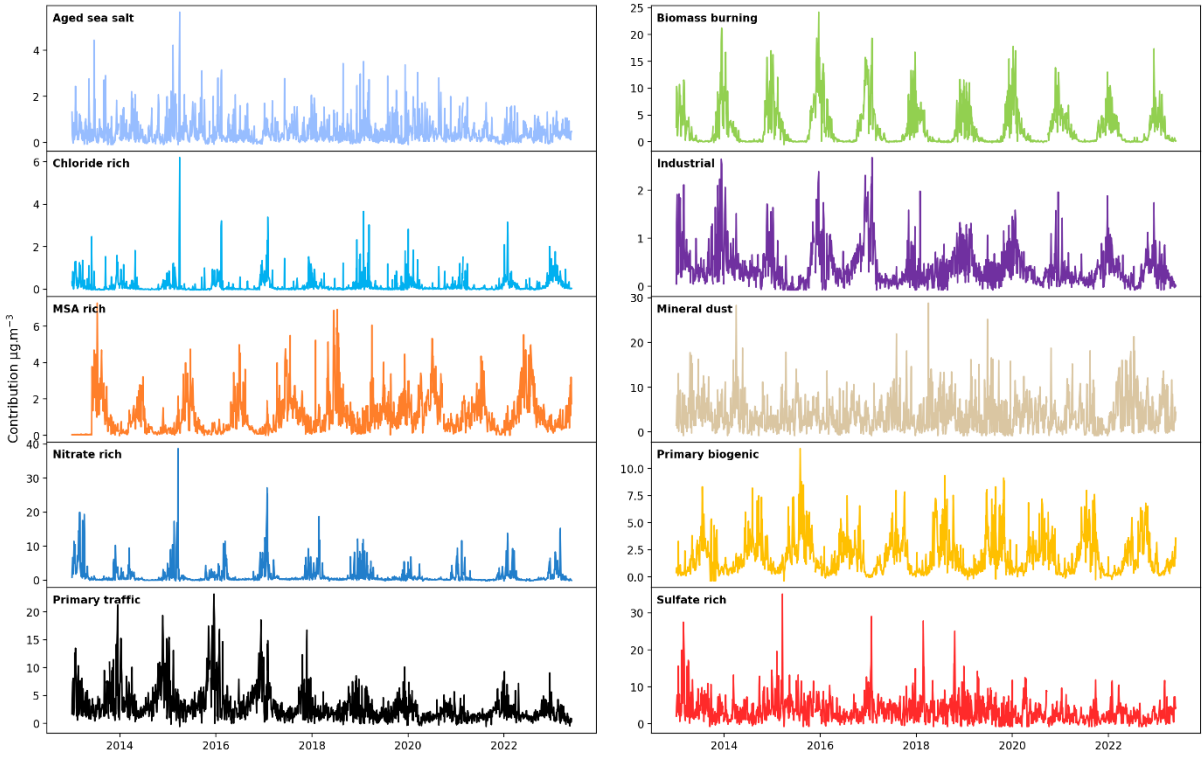

Figure S4. Temporal evolution of PM sources, solution 11 years

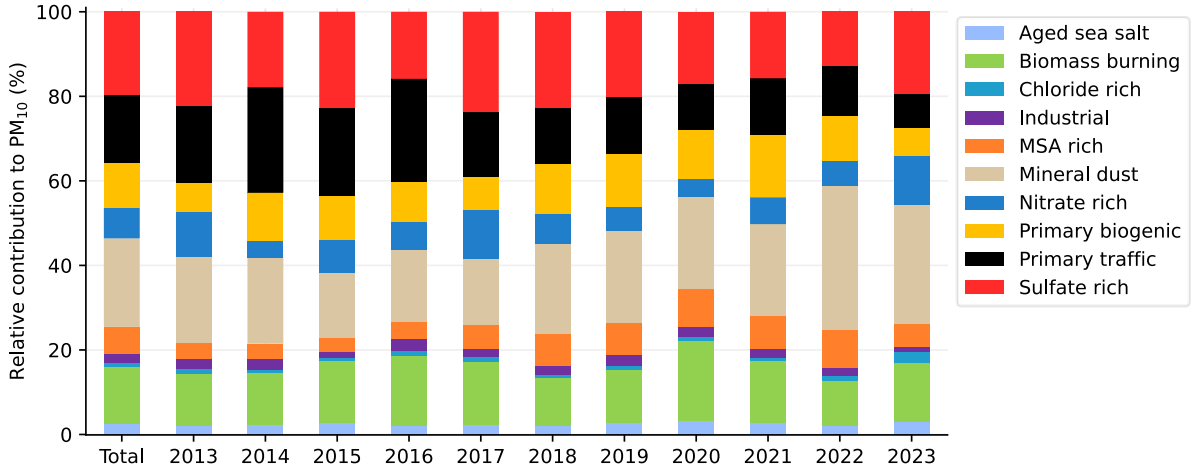

Figure S5. The absolute average contribution of sources to PM_{10} (%) for 11 years and every years.

S6. Tendency of PM_{10} and NOx

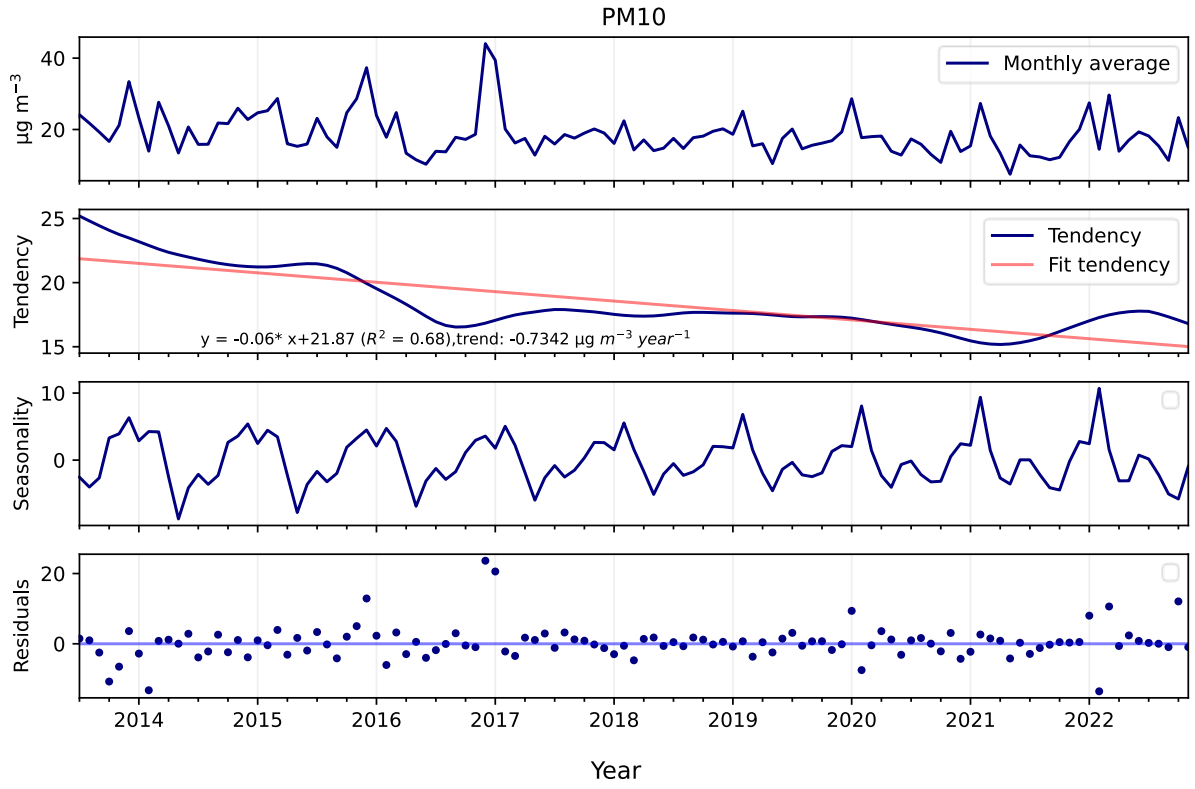

Figure S6. STL decomposition of PM_{10}

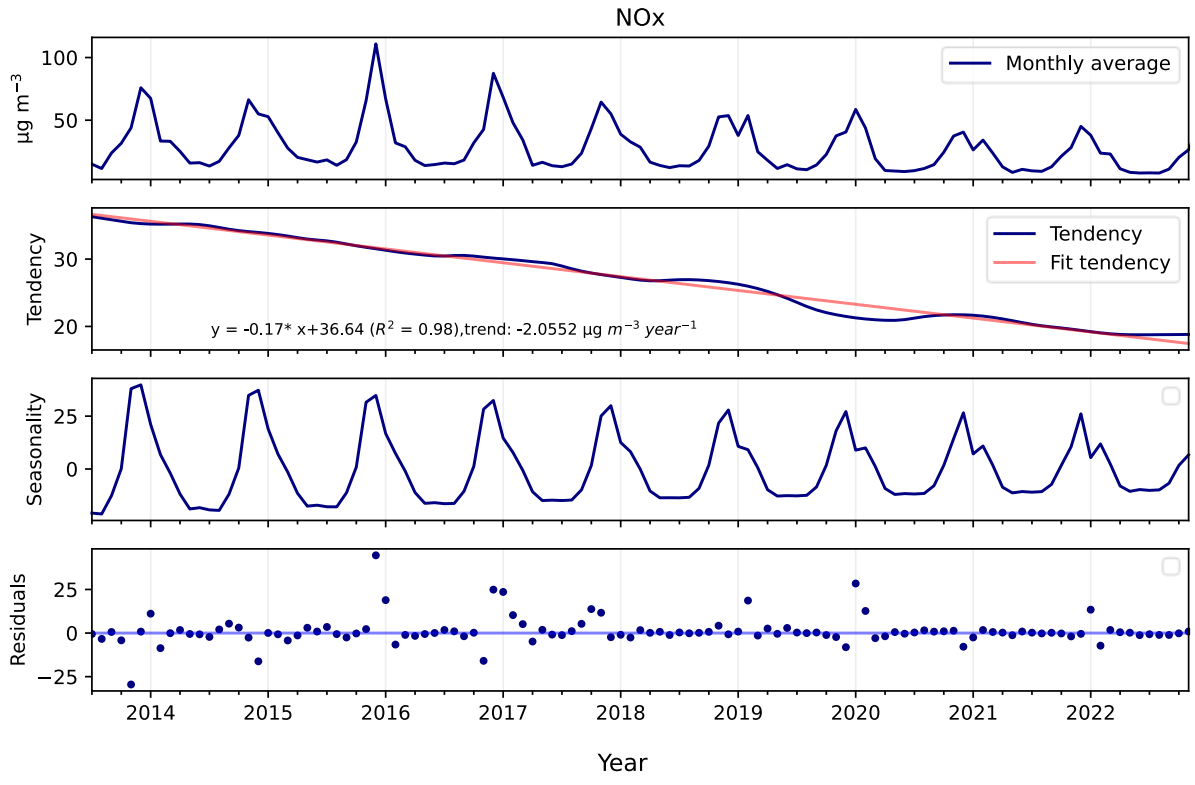

Figure S7. STL decomposition of NO_x

S7. Thermal inversion analysis

This analysis is conducted for the period Nov 2017 to May 2023, when the measurements on the mountain slopes are available. A good correlation is obtained between the PM_{10} and bulk temperature at the city level (r reaching 0.6, p<<0.001) for the winter months and it is even better when considering only the persistent inversion periods (r reaching 0.7, p<<0.001) for individual years (Table S7). Interestingly, the bivariate distribution between the daily PM_{10} concentration and daily average $\Delta T/\Delta z$ in winter months revealed that the majority of PM_{10} concentration peaks (exceedances above 40 µg m^{-3}) are from persistent inversion (Figure S8). The distribution of the day without and with persistent inversion (Figure S9) also shows that a few high PM_{10} concentration could be found in the days without persistent inversion, meanwhile a day with persistent inversion is not always associated to a high PM_{10} concentration. This result is not surprising, since the concentration of PM_{10} also depend on other meteorological conditions (precipitation, heat deficit) as well as variations in pollutant emissions (Carbone et al., 2010; Largeron and Staquet, 2016).

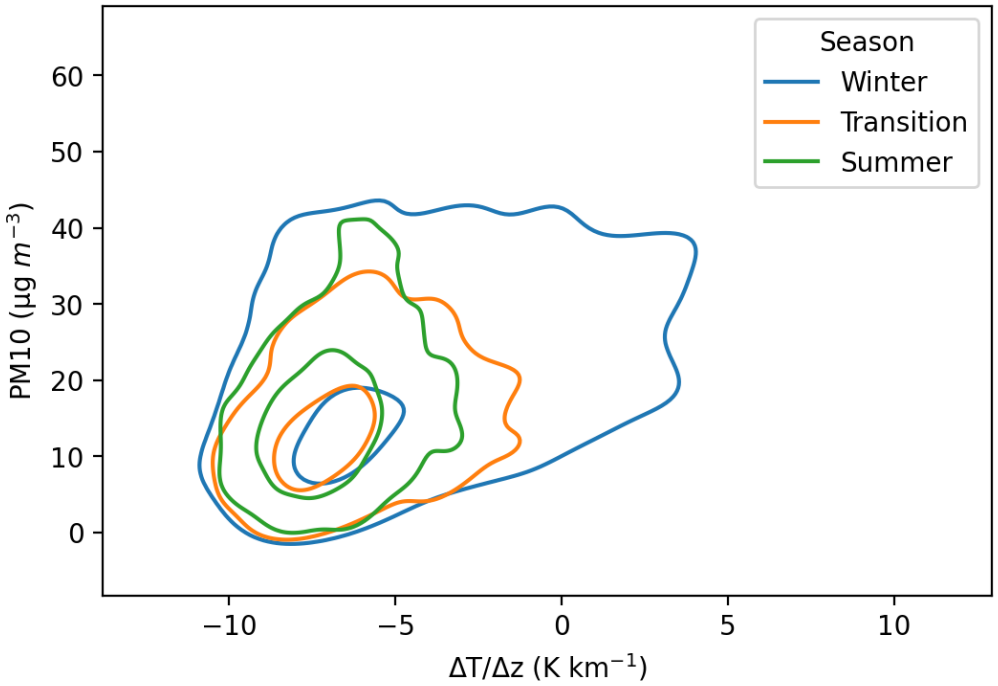

Figure S8. Bivariate distribution between PM10 and bulk temperature in winter (blue contour, for the month of Dec, Jan, Feb), summer (green contour for the month of Jun, Jul, Aug) and transition season (orange contour for the remaining months).

Table S 7. Correlation between PM and bulk temperature in winter and in persistent inversion period. The star repressing the p-value. (* : < 0.001, **: < 0.01, * < 0.05, "ns": non-significant)**

	R^2 in winter	R^2 in persistent inversion period
2017	0.60**	0.50**
2018	0.19*	0.47**
2019	0.50***	0.33**
2020	0.57***	0.47***
2021	0.50***	0.67**
2022	0.30***	0.22*
2023	0.05 ns	0.05 ns

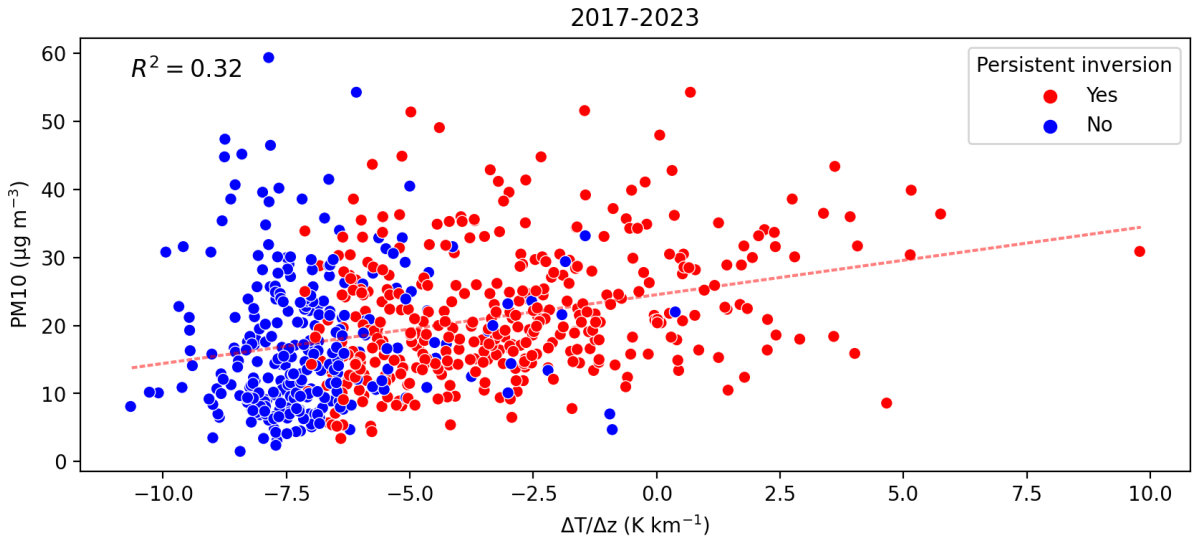

Figure S9. Daily PM_{10} concentration and daily average $\Delta T/\Delta z$ in winter months (from November to March) for the period of 2017 to 2023. The red points represent the winter days when the persistent inversion is detected, and the blue points represent the other winter days.

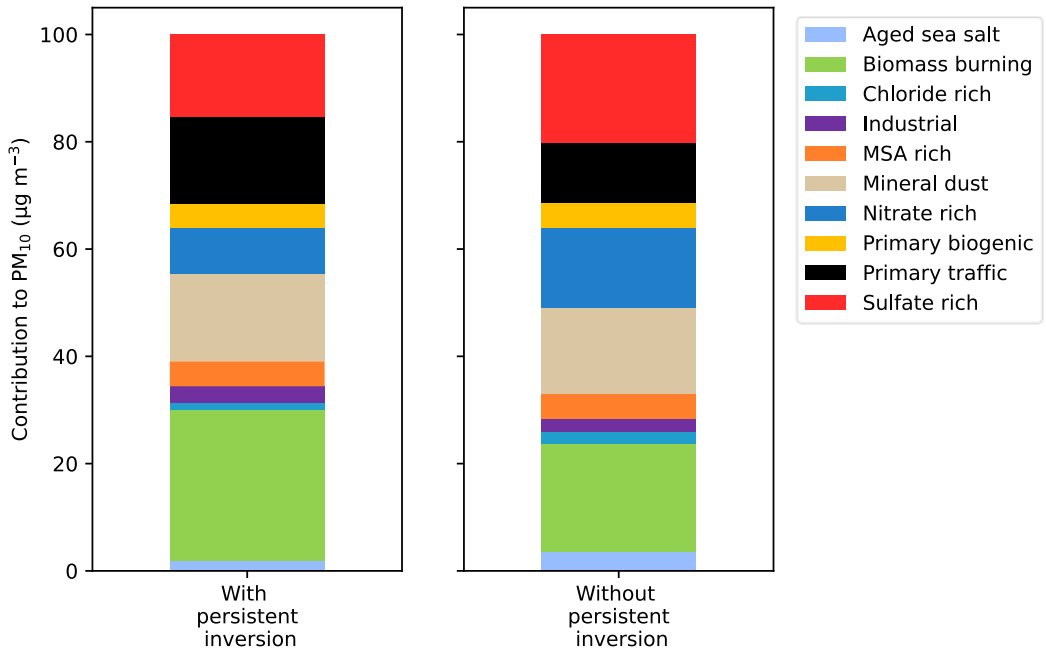

Figure S10. Relative contribution of the different sources to PM_{10} for days with persistent inversion vs non-inversion days of the winters 2017-2023.

Thermal inversion events were used to evaluate the relationship between biomass burning influence onPM_{10} concentration and meteorological conditions. As shown in Figure S9, more than half of the high PM_{10} concentration event is related to persistent inversion. Especially for biomass burning, which is emitted principally in winter, could be highly enlarged under the influence of inversion. Figure 7 presents the contribution of biomass burning and the bulk temperature in winter, reveals that 41% of the biomass burning contribution is explained by the temperature gradient ($\Delta T/\Delta z$) between 2017 and 2023. better than considering PM_{10} (R^2 = 0.3). In particular, the high contribution of biomass burning (>10 µg m^{-3}) is always found in the episodes of persistent inversion. This demonstrates that the occurrence of persistent inversion systematically decreasing the temperature in the city enhances the use of heating as well as traps the aerosol and enlarges the contribution of biomass burning. Although the relationship between persistent inversion events and biomass burning emissions is affirmed, the reduction trend of biomass burning does not completely depend on the persistent inversion events. As shown in Figure 5, the number of persistent inversions per year is nearly similar, while the contribution of biomass burning steadily decreases over the years. The average annual biomass burning sources PMF-derived is compared to the local PM_{10} emission inventory by residential heating (tonnes), provided by the Central air quality monitoring laboratory (Atmo AuRA) to confirm the trend of biomass burning. The annual average of biomass burning is agreed with the emission inventory, demonstrating the consistency between the sources observed by the PMF model and the local inventory emission data. Since 2015, the Grenoble Metropolis has set up an air-wood bonus to encourage households to renew their individual wood-burning appliance (fireplace or stove), and aim to replace all open fireplaces with closed appliances in October 2024. The downward trend of biomass burning demonstrates the effectiveness of the region's policy in changing residential heating equipment, to improve the city's air quality.

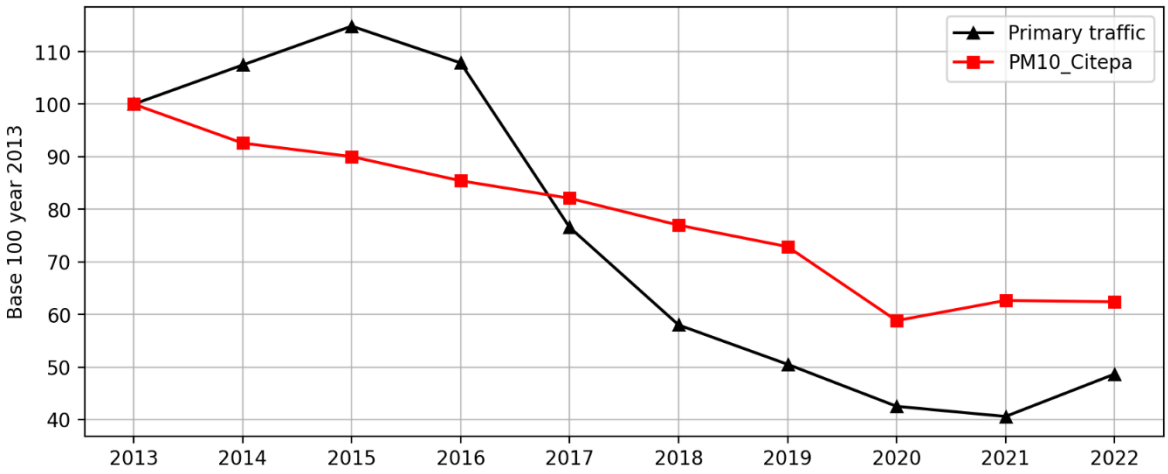

Figure S11. Comparison of the traffic contribution and PM10 emission by the transport sector in France.

S8. OP PM10 SA result

Table S 8. The appropriate model of OP SA

	OP_{AA}	OP_{DTT}
Heteroscedasticity	Yes	Yes
Collinearity	No	No
The suitable model	wPLS, WLS	wPLS, WLS

Table S 9. The R^2, RMSE and MAE of the suitable models

	OP_{AA}		OP_{DTT}	
	wPLR	**WLS**	**wPLR**	**WLS**
R^2	0.69	0.70	0.61	0.61
RMSE	0.88	0.85	0.89	0.86
MAE	0.49	0.47	0.63	0.62

Tendency of OP_m and OP_v

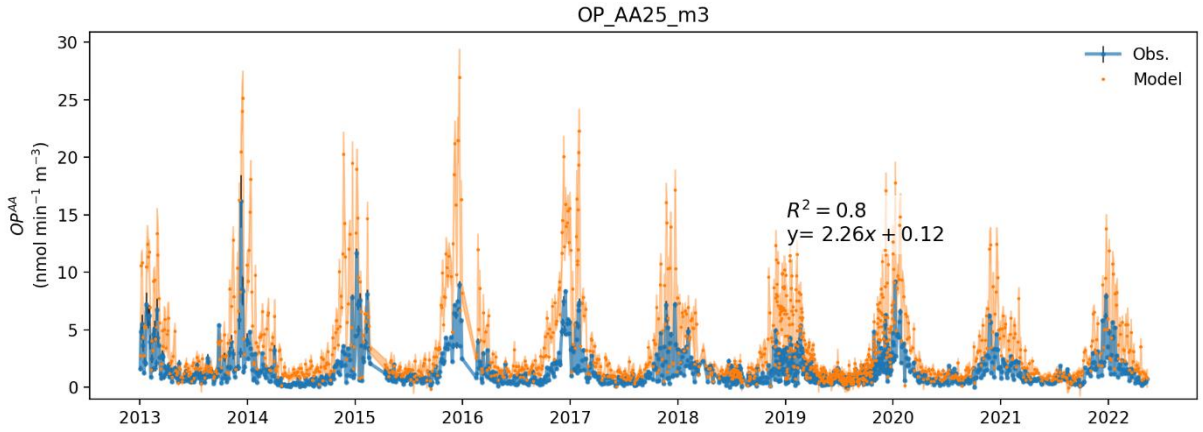

Figure S12. The comparison between observed OP_{AA} and predicted OP_{AA}

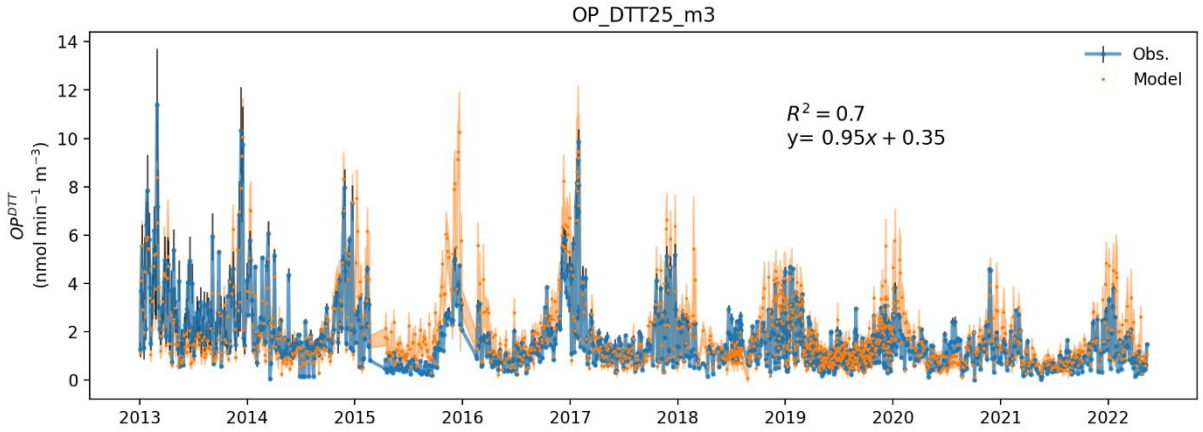

Figure S13. The comparison between observed OP_{DTT} and predicted OP_{DTT}

Table S 10. Accuracy metric of the testing and training dataset of Multiple layer perceptron (MLP) and Random Forest (RF)

	MLP		RF	
	Training	**Testing**	**Training**	**Testing**
R^2	0.75	0.75	0.90	0.72
RMSE	0.67	0.74	0.32	0.79
MAE	0.36	0.39	0.17	0.41

Table S 11. Intrinsic OP_{AA} and intrinsic OP_{DTT} description

OPtype	Source	count	mean	std	min	25%	50%	75%	max	IQR
AA	Aged sea salt	500	-0.02	0.07	-0.23	-0.06	-0.03	0.00	0.19	0.06
	Biomass burning	500	0.76	0.13	0.48	0.67	0.74	0.82	1.22	0.15
	Chloride rich	500	-0.07	0.09	-0.32	-0.09	-0.05	-0.02	0.18	0.07
	Industrial	500	0.48	0.14	-0.04	0.44	0.52	0.57	0.74	0.12
	MSA rich	500	0.20	0.04	0.03	0.18	0.20	0.23	0.30	0.05
	Mineral dust	500	-0.03	0.06	-0.17	-0.07	-0.04	0.01	0.19	0.07
	Nitrate rich	500	0.09	0.16	-0.43	0.00	0.13	0.20	0.51	0.20
	Primary biogenic	500	0.00	0.04	-0.11	-0.02	0.00	0.03	0.10	0.05
	Primary traffic	500	0.38	0.10	0.02	0.32	0.38	0.46	0.67	0.14
	Sulfate rich	500	-0.01	0.08	-0.22	-0.05	-0.02	0.04	0.23	0.09
DTT	Aged sea salt	500	0.03	0.02	0.00	0.02	0.03	0.05	0.13	0.02
	Biomass burning	500	0.14	0.09	0.00	0.08	0.13	0.17	0.45	0.09
	Chloride rich	500	0.01	0.02	0.00	0.00	0.00	0.00	0.12	0.00
	Industrial	500	0.52	0.08	0.31	0.47	0.51	0.55	0.86	0.08
	MSA rich	500	0.01	0.02	0.00	0.00	0.00	0.02	0.13	0.02
	Mineral dust	500	0.01	0.02	0.00	0.00	0.00	0.00	0.17	0.00
	Nitrate rich	500	0.11	0.12	0.00	0.02	0.07	0.12	0.50	0.10
	Primary biogenic	500	0.02	0.03	0.00	0.00	0.01	0.02	0.12	0.02
	Primary traffic	500	0.24	0.07	0.06	0.20	0.24	0.28	0.48	0.08
	Sulfate rich	500	0.09	0.04	0.00	0.06	0.08	0.11	0.22	0.05

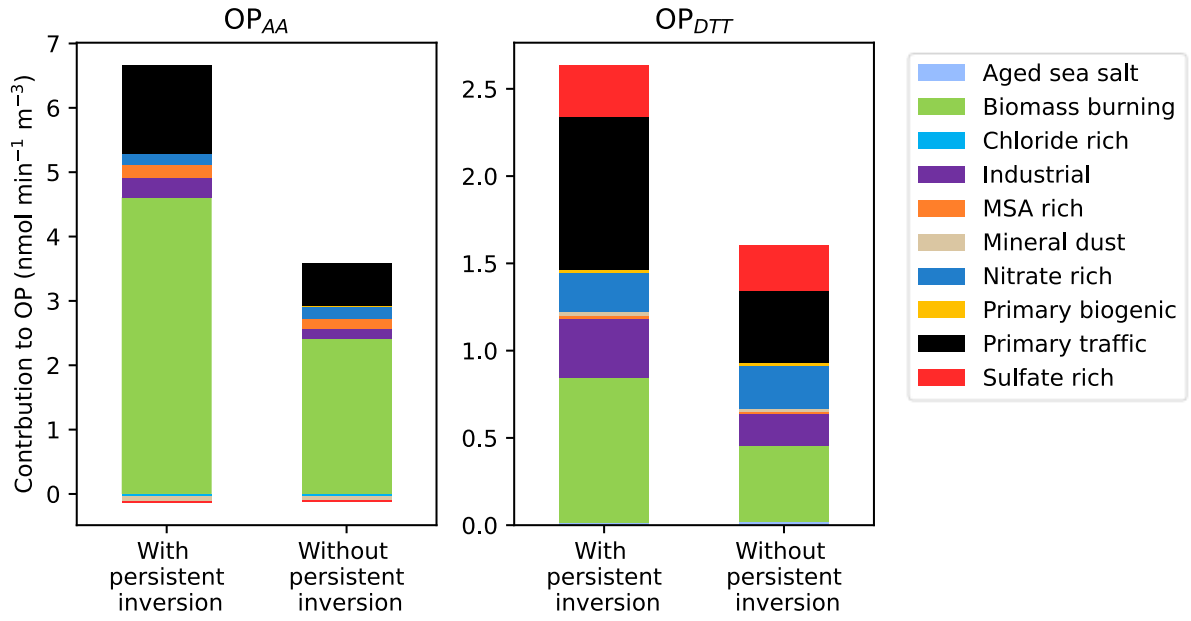

Figure S14. Contribution of the different sources to OP_v^{AA} (left) and OP_v^{DTT} (right), for days with persistent inversion vs non-inversion days of the winters 2017-2023.

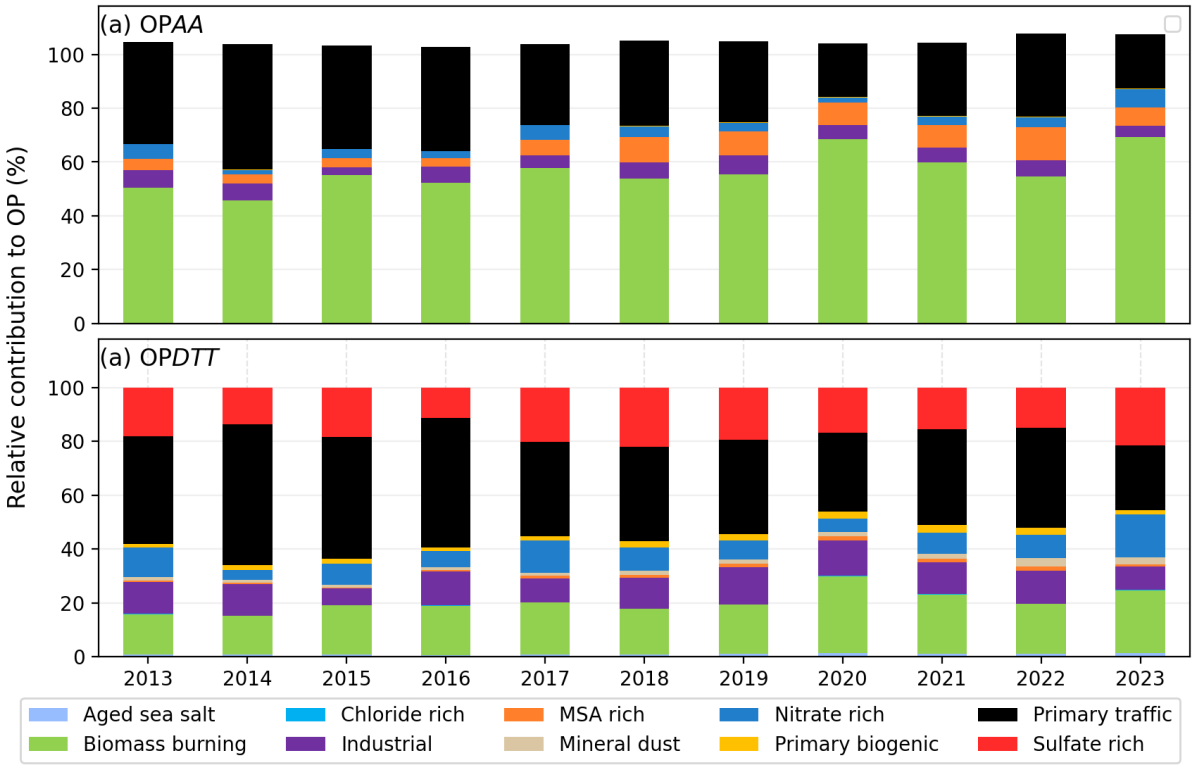

Figure S15. Yearly average relative contribution of sources to (a) OP_{AA}^v and (b) OP_{DTT}^v

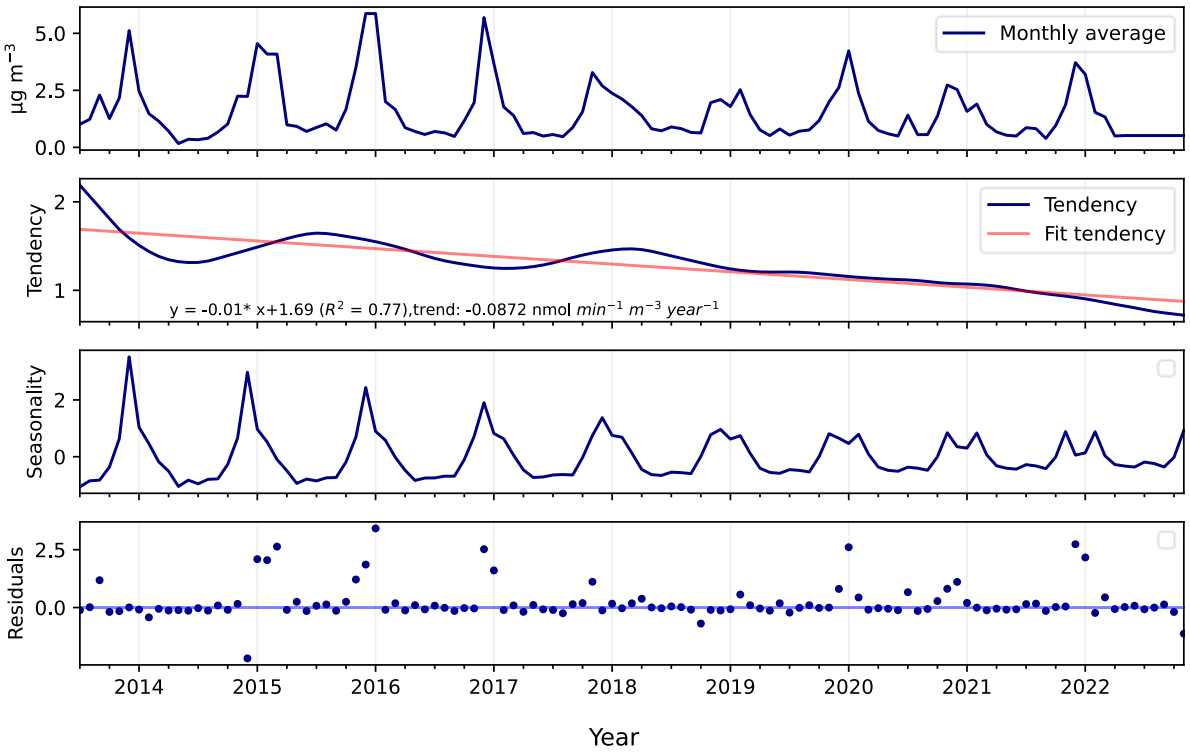

Figure S16. STL decomposition of OP_{AA}^{m}

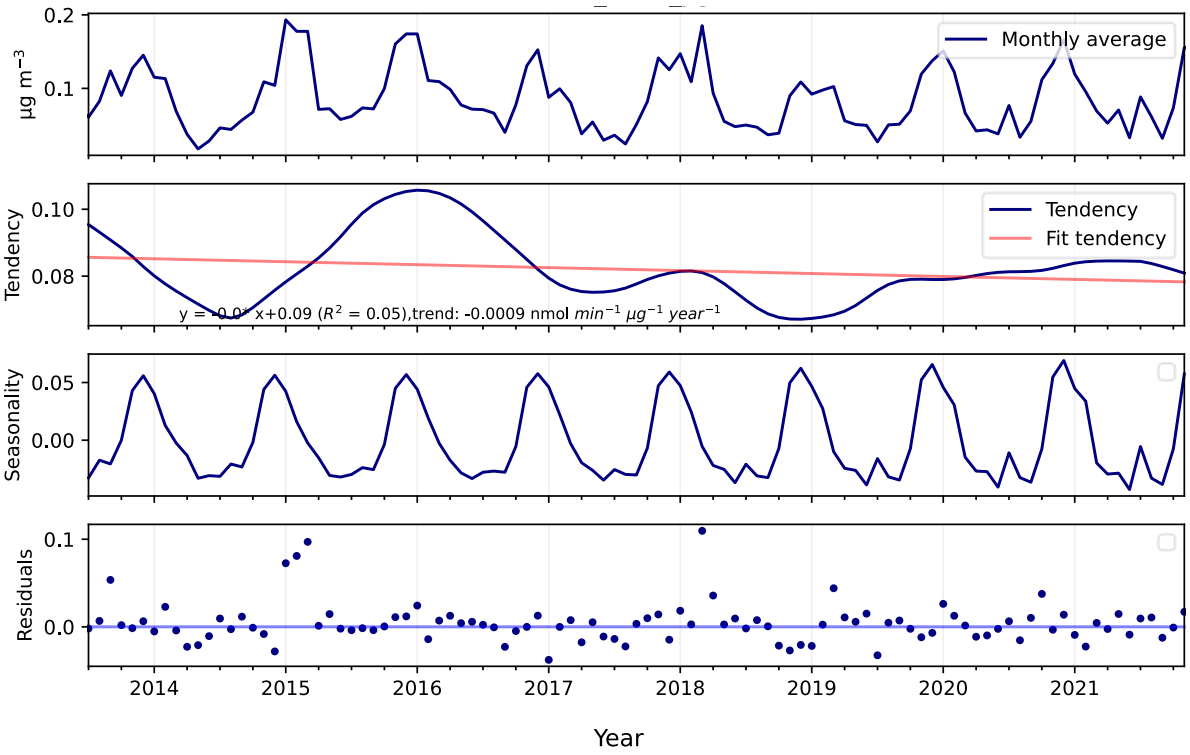

Figure S17. STL decomposition of OP_{AA}^{v}

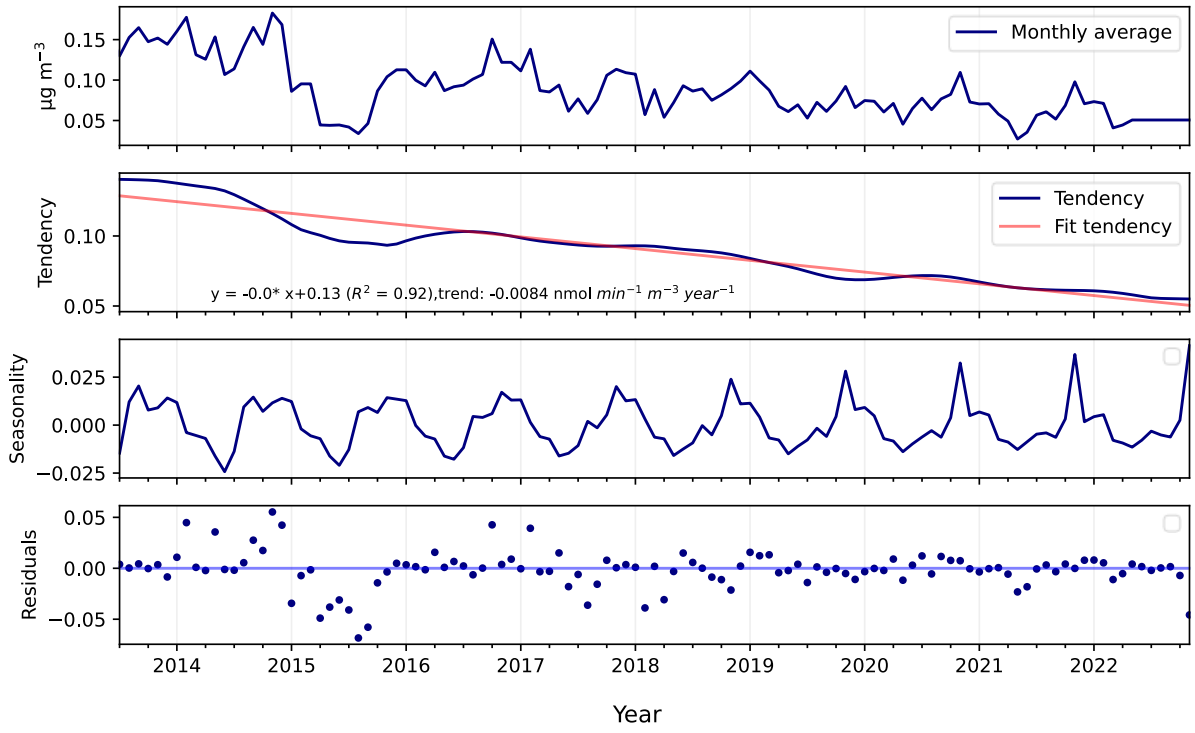

Figure S18. STL decomposition of OP_{DTT}^{m}

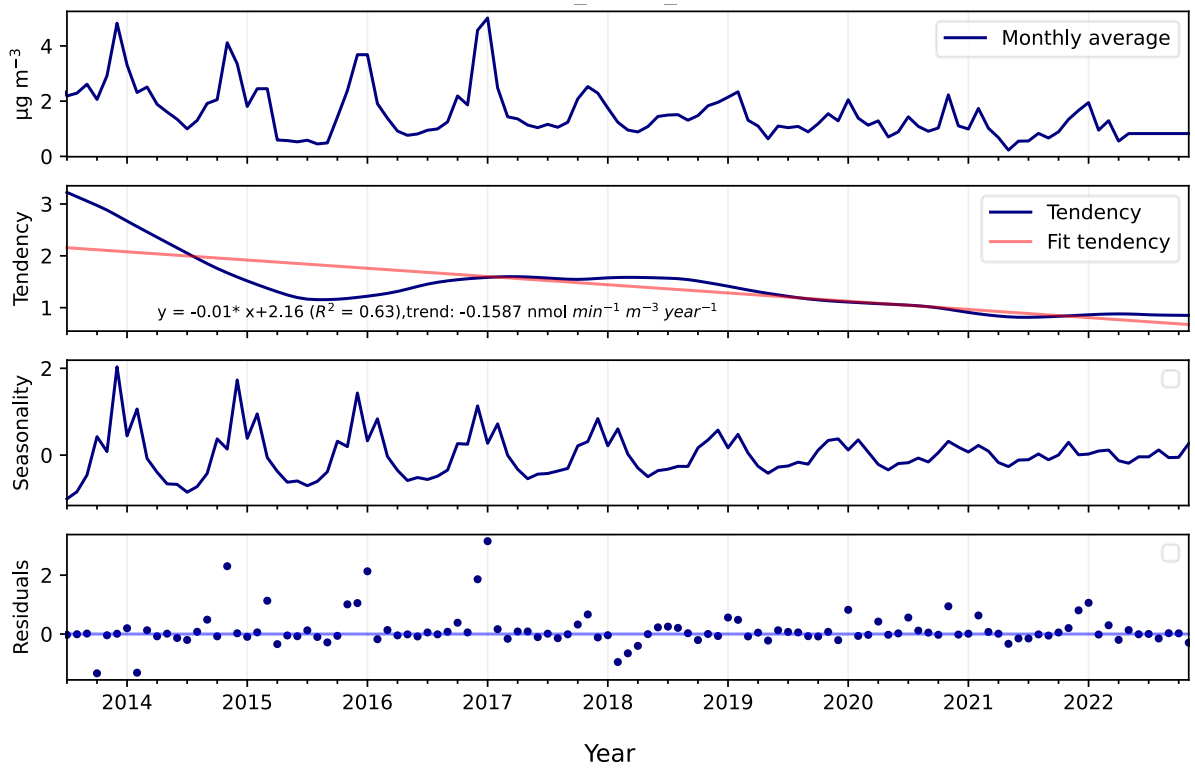

Figure S19. STL decomposition of OP_{DTT}^{v}

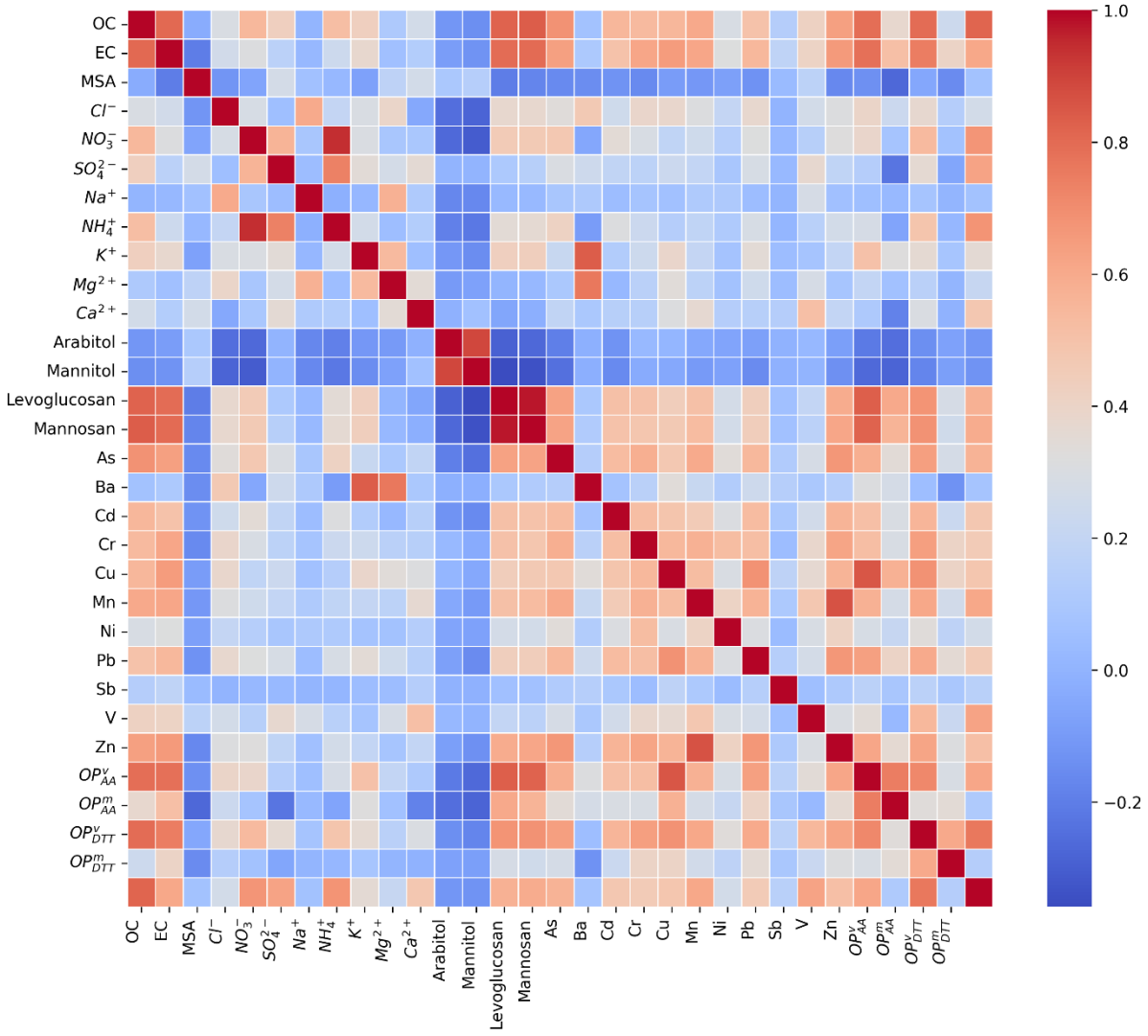

Figure S20. Heat map correlation between PM compositions and OP

References

Alexander, B., Park, R. J., Jacob, D. J., Li, Q. B., Yantosca, R. M., Savarino, J., Lee, C. C. W., and Thiemens, M. H.: Sulfate formation in sea-salt aerosols: Constraints from oxygen isotopes, J. Geophys. Res. Atmospheres, 110, 2004JD005659, https://doi.org/10.1029/2004JD005659, 2005.

Azur, M. J., Stuart, E. A., Frangakis, C., and Leaf, P. J.: Multiple imputation by chained equations: what is it and how does it work?, Int. J. Methods Psychiatr. Res., 20, 40–49, https://doi.org/10.1002/mpr.329, 2011.

Belis, C. A., Favez, O., Harrison, R. M., Larsen, B. R., Amato, F., El Haddad, I., Hopke, P. K., Nava, S., Paatero, P., Prévôt, A., Quass, U., Vecchi, R., Viana, M., and European Commission (Eds.): European guide on air pollution source apportionment with receptor models, Publications Office, Luxembourg, 1 pp., https://doi.org/10.2788/9332, 2014.

Carbone, C., Decesari, S., Mircea, M., Giulianelli, L., Finessi, E., Rinaldi, M., Fuzzi, S., Marinoni, A., Duchi, R., Perrino, C., Sargolini, T., Vardè, M., Sprovieri, F., Gobbi, G. P., Angelini, F., and Facchini, M. C.: Size-resolved aerosol chemical composition over the Italian Peninsula during typical summer and winter conditions, Atmos. Environ., 44, 5269–5278, https://doi.org/10.1016/j.atmosenv.2010.08.008, 2010.

Favez, O., El Haddad, I., Piot, C., Boréave, A., Abidi, E., Marchand, N., Jaffrezo, J. L., Besombes, J. L., Personnaz, M. B., Sciare, J., Wortham, H., George, C., and D'Anna, B.: Inter-comparison of source apportionment models

for the estimation of wood burning aerosols during wintertime in an Alpine city (Grenoble, France), Atmospheric Chem. Phys., 10, 5295–5314, https://doi.org/10.5194/acp-10-5295-2010, 2010.

Largeron, Y. and Staquet, C.: Persistent inversion dynamics and wintertime PM10 air pollution in Alpine valleys, Atmos. Environ., 135, 92–108, https://doi.org/10.1016/j.atmosenv.2016.03.045, 2016.

Ocepek, U., Rugelj, J., and Bosnić, Z.: Improving matrix factorization recommendations for examples in cold start, Expert Syst. Appl., 42, 6784–6794, https://doi.org/10.1016/j.eswa.2015.04.071, 2015.

Pedregosa, F., Varoquaux, G., Gramfort, A., Michel, V., Thirion, B., Grisel, O., Blondel, M., Prettenhofer, P., Weiss, R., Dubourg, V., Vanderplas, J., Passos, A., Cournapeau, D., Brucher, M., Perrot, M., and Duchesnay, E.: Scikit-learn: Machine Learning in {P}ython, J. Mach. Learn. Res., 12, 2825–2830, 2011.

Putaud, J.-P., Raes, F., Van Dingenen, R., Brüggemann, E., Facchini, M.-C., Decesari, S., Fuzzi, S., Gehrig, R., Hüglin, C., Laj, P., Lorbeer, G., Maenhaut, W., Mihalopoulos, N., Müller, K., Querol, X., Rodriguez, S., Schneider, J., Spindler, G., Brink, H. T., Tørseth, K., and Wiedensohler, A.: A European aerosol phenomenology—2: chemical characteristics of particulate matter at kerbside, urban, rural and background sites in Europe, Atmos. Environ., 38, 2579–2595, https://doi.org/10.1016/j.atmosenv.2004.01.041, 2004.

Putaud, J.-P., Van Dingenen, R., Alastuey, A., Bauer, H., Birmili, W., Cyrys, J., Flentje, H., Fuzzi, S., Gehrig, R., Hansson, H. C., Harrison, R. M., Herrmann, H., Hitzenberger, R., Hüglin, C., Jones, A. M., Kasper-Giebl, A., Kiss, G., Kousa, A., Kuhlbusch, T. A. J., Löschau, G., Maenhaut, W., Molnar, A., Moreno, T., Pekkanen, J., Perrino, C., Pitz, M., Puxbaum, H., Querol, X., Rodriguez, S., Salma, I., Schwarz, J., Smolik, J., Schneider, J., Spindler, G., Ten Brink, H., Tursic, J., Viana, M., Wiedensohler, A., and Raes, F.: A European aerosol phenomenology – 3: Physical and chemical characteristics of particulate matter from 60 rural, urban, and kerbside sites across Europe, Atmos. Environ., 44, 1308–1320, https://doi.org/10.1016/j.atmosenv.2009.12.011, 2010.

Salameh, D., Detournay, A., Pey, J., Pérez, N., Liguori, F., Saraga, D., Bove, M. C., Brotto, P., Cassola, F., Massabò, D., Latella, A., Pillon, S., Formenton, G., Patti, S., Armengaud, A., Piga, D., Jaffrezo, J. L., Bartzis, J., Tolis, E., Prati, P., Querol, X., Wortham, H., and Marchand, N.: PM2.5 chemical composition in five European Mediterranean cities: A 1-year study, Atmospheric Res., 155, 102–117, https://doi.org/10.1016/j.atmosres.2014.12.001, 2015.